



OPEN

SUBJECT AREAS:

BATTERIES
NANOWIRESReceived
27 June 2014Accepted
9 October 2014Published
3 November 2014

Correspondence and requests for materials should be addressed to J.-G.P. (jgpark@kist.re.kr) or D.-W.K. (dwkim1@korea.ac.kr)

Germanium microflower-on-nanostem as a high-performance lithium ion battery electrode

Gwang-Hee Lee^{1,3}, S. Joon Kwon¹, Kyung-Soo Park¹, Jin-Gu Kang¹, Jae-Gwan Park¹, Sungjun Lee², Jae-Chan Kim³, Hyun-Woo Shim³ & Dong-Wan Kim³

¹Institute for Multi-Convergence of Matter (IMCM), Korea Institute of Science and Technology (KIST), Seoul 136-791, Korea, ²Division of Physical Metrology, Korea Research Institute of Standards and Science, Daejeon 305-340, Korea, ³School of Civil, Environmental and Architectural Engineering, Korea University, Seoul 136-713, Korea.

We demonstrate a new design of Ge-based electrodes comprising three-dimensional (3-D) spherical microflowers containing crystalline nanorod networks on sturdy 1-D nanostems directly grown on a metallic current collector by facile thermal evaporation. The Ge nanorod networks were observed to self-replicate their tetrahedron structures and form a diamond cubic lattice-like inner network. After etching and subsequent carbon coating, the treated Ge nanostructures provide good electrical conductivity and are resistant to gradual deterioration, resulting in superior electrochemical performance as anode materials for LIBs, with a charge capacity retention of 96% after 100 cycles and a high specific capacity of 1360 mA h g⁻¹ at 1 C and a high-rate capability with reversible capacities of 1080 and 850 mA h g⁻¹ at the rates of 5 and 10 C, respectively. The improved electrochemical performance can be attributed to the fast electron transport and good strain accommodation of the carbon-filled Ge microflower-on-nanostem hybrid electrode.

The evolution of portable electronic and consumer devices has steered research interests toward scientific and technological efforts in this field; consequently, many studies have focused on controlling the morphology and architecture of nanostructures, along with the integration of nanoscale building blocks into three-dimensional (3-D) architectures^{1,2}.

In the past, morphology control using various self-organized nanostructures such as nanowires³⁻⁶, nanorods⁷⁻⁹, nanotubes^{10,11}, cubes^{12,13}, sheets^{14,15}, spheres¹⁶, and dendrites^{17,18} was highly desirable for the development of gas sensors, light-emitting diodes, energy-harvesting devices, and energy-storage devices. However, compared to conventional one-dimensional (1-D) nanostructures, 3-D microscale/1-D nanoscale hybrid structures show greater promise in many advanced devices in fields such as chemistry, physics, biology, and medicine, as well as in molecular devices¹⁹⁻²⁶, because of the tunability of the properties via substitution by various functional groups and the reduced agglomeration between the individual 1-D nanostructures.

Of these microscale/nanoscale hybrid structures, 3-D network-based nanostructures are particularly attractive. As these structures are composed of highly ordered 3-D hierarchical assemblies built from homogeneous and continuous 1-D nanorods, tailoring these structures will help improve transport properties such as electrical conductivity, heat conduction, and fluid flow^{21,27}. In general, crystal growth that exhibits polytypism occurs by either microscopic interfacial anisotropy such as different surface energies of the different crystalline facets or nonlinear instability at the atomic boundary scale^{28,29}.

In particular, a spatial gradient of the precursor concentration fields as the driving force of diffusion under anisotropic interfacial instabilities and the resulting pattern formation out of equilibrium would promote the growth of a multipod structure. Although it is highly desirable to use multipod nanostructures for energy-transfer or energy-storage materials, the ability to prepare such structures is limited³⁰. Instead of conventional preparation approaches, it would be appropriate to employ a mechanism for the formation of self-replicating polytip structures under polytypism.

In the present work, we develop a novel, facile, template-free, thermal evaporation method to prepare self-supported 3-D Ge network-based nanostructured arrays on a current-collecting substrate. The fabricated 3-D Ge fractal nanorod network structures are 3-D microscale/1-D nanoscale hybrid structures, consisting of networked Ge microflower on a Ge “backbone” nanostem (Ge MF-on-NS hybrids). The Ge microflowers were observed to

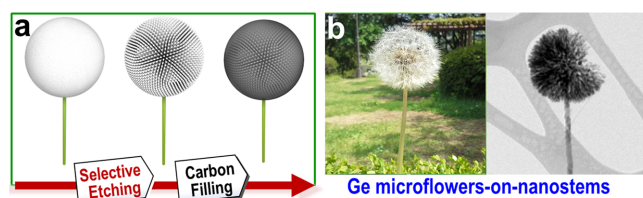


Figure 1 | Schematic illustration of Ge MF-on-NS hybrid assemblies. (a) Synthesis of Ge MF-on-NS hybrids, involving selective etching and carbon-filling processes. The simplified illustration was drawn by J.-C. Kim and D.-W. Kim. (b) Ge MF-on-NS hybrid after etching the GeO_x sheath, giving the appearance of a dandelion. The digital photograph (left) and transmission electron microscopy image (right) were taken from G.-H. Lee.

self-replicate Ge tetrahedrons in an organized manner, which results in a diamond cubic lattice-like network structure with periodic porosity. After the selective etching of an amorphous GeO_x sheath from each Ge nanorods in the microflowers, the porous Ge network acts as a scaffold for a carbon coating, which opens efficient electronic pathways of active materials to the current collector. When used as anodes for lithium ion batteries (LIBs) without any ancillary materials, the carbon-filled Ge MF-on-NS hybrids manifest an excellent rate capability and a significantly enhanced cycling performance.

Results

Synthesis of Ge microsphere-on-nanostem hybrids. The synthetic process for Ge MF-on-NS hybrids is depicted in Fig. 1a. Firstly, 3-D Ge microsphere-on-nanostem (SP-on-NS) hybrids were synthesized by thermal evaporation of germanium powder. Because of spontaneous and rapid oxidation, the as-grown Ge SP-on-NS hybrids are covered with an amorphous GeO_x sheath. Next, selective etching dissolved most of the GeO_x sheath, leaving crystalline Ge. The etching process is selective because of the differences in the water solubility of Ge and GeO_x . As shown in Supplementary Fig. S1, Germanium oxides are soluble in water^{31–33}. The etching of the Ge SP-on-NS hybrids by aqueous solution results in the selective removal of the GeO_x sheath and the formation of complex structures resembling a dandelion (Fig. 1b). Carbon filling of the Ge MF-on-NS hybrids was carried out by the decomposition of citric acid solution.

The morphology of the Ge SP-on-NS hybrids before etching was investigated by field emission scanning electron microscopy (FESEM) and transmission electron microscopy (TEM). The FESEM image shows that the Ge SP-on-NS hybrids are composed of nanostems and microspheres (Fig. 2a). A low-resolution TEM image showing the morphology of the individual Ge SP-on-NS hybrids is presented in Fig. 2b, in which both a Ge microsphere and an underlying nanowire segment can be clearly seen. The Ge microsphere is attached to the tip of the nanowire. Furthermore, a high-angle annular dark-field (HAADF) scanning TEM (STEM) image was recorded to visualize the contrast between the dark and bright materials (Fig. 2c) and reveals that the interior of the Ge microsphere is actually composed of needle-shaped structures and is not porous. Energy-dispersive X-ray spectroscopy (EDS) analysis (bottom part of Fig. 2d) confirms that the Ge microsphere consists of Ge and O. Hence, the “dark” domain of the Ge microsphere in Fig. 2c is presumed to be germanium oxide (GeO_x). Furthermore, the dispersed selected-area electron diffraction (SAED) pattern (upper-right part of Fig. 2d) shows that the needle-shaped structures of the Ge microsphere are crystalline Ge, which agrees with the high-resolution TEM (HRTEM) results in Fig. 2e. The measured interplanar distance of the microsphere is 0.329 nm, which corresponds to the (111) planes. Figure 2f shows a typical TEM image and the corresponding EDS line-scan profile of Ge and O across a Ge nanos-

tem. These results demonstrate that the Ge nanostem is an amorphous GeO_x /crystalline Ge sheath/core nanostem. The SAED pattern of the Ge nanostem (upper-left part of Fig. 2d) indicates that the core of the Ge nanostem has a perfect single-crystalline structure of cubic Ge, which corresponds to the (111), (311), and (400) planes. In addition, the X-ray diffraction (XRD) patterns of the as-grown Ge SP-on-NS hybrids and the Au-coated stainless steel (SS) substrate are displayed in Supplementary Fig. S2. With the exception of the two peaks of the SS substrate, the Ge SP-on-NS hybrids contain cubic Ge phase (face-centered cubic (*fcc*), PDF No. 03-065-0333) in addition to a small amount of the cubic Au phase (*fcc*, PDF No. 03-065-2870), $\beta\text{-Au}_{0.72}\text{Ge}_{0.28}$ phase (hexagonal, PDF No. 03-065-8616), and cubic $\text{Fe}_{0.84}\text{Ge}_{0.16}$ phase (*fcc*, PDF No. 00-017-0245). The peaks of the cubic Au phase and the $\beta\text{-Au}_{0.72}\text{Ge}_{0.28}$ phase are due to the Au thin film used as a catalyst, and the peaks of the cubic $\text{Fe}_{0.84}\text{Ge}_{0.18}$ phase arise from the SS substrate.

The dependence of the formation of the Ge SP-on-NS hybrids on the growth conditions was investigated in detail. Supplementary Figures S3 and S4 show the Au thickness and temperature dependences of the Ge SP-on-NS hybrid formation. As the Au thickness increases on the SS substrate, the density of the products becomes higher (Supplementary Fig. S3). As the synthesis temperature in the furnace decreases (Supplementary Fig. S4a), there is a systematic trend, with the formation of nanowires at 597–576°C, a mixture of nanowires and microspheres at 576–454°C, and microspheres being formed at 454–384°C (Supplementary Figs. S4b–f). In the case of the growth of nanowires, Au nanoparticles were found attached to the tips of the synthesized nanowires, confirming that their growth was governed by a typical vapor–liquid–solid (VLS) mechanism (Supplementary Fig. S5).

To study the self-replicated structure formation of the 3-D Ge nanorod network structure during the formation of the microsphere, we employed a focused ion beam (FIB), which examines the cross-sectional morphology of the microsphere (Fig. 3a). The Ge microspheres are structurally well integrated with the Ge needle-shaped structures, as supported by the medium-magnification TEM image of the cross section (Fig. 3b). We observed that the inner structure of the Ge microsphere can be formed by the self-replication of tetrahedral Ge nanorods. As apparent from Fig. 3b, the Ge needle-shaped structures are encapsulated within the GeO_x sheath. The HRTEM image reveals that the Ge needle-shaped structures are crystalline, and the encompassing GeO_x sheath is completely amorphous (Fig. 3c). The interplanar crystal distance in the Ge needle-shaped structures is *ca.* 0.330 nm, which corresponds to the (111) planes of Ge. We observe that the interplanar angles between the {111} facets are *ca.* 109.5°, with a tetrahedral symmetry of diamond cubic structures. The diamond cubic structures occur because the two atoms at 000 and $\frac{1}{4}\frac{1}{4}\frac{1}{4}$ are at the center of a regular tetrahedron, with sp^3 hybrid covalent bonds connecting them to the atoms at the corners of the tetrahedron. The atomic bond directions of the tetrahedron are in all the [111] directions, at equal angles of *ca.* 109.5°.

The 3-D structure of the Ge microspheres examined by TEM and FIB appears to be a network structure. Notably, however, the observed network structure is distinguished from other self-similar structures observed in various physical and chemical systems, including the diffusion- (DLA) or reaction-limited aggregation (RLA) or dendritic morphology of organic crystals. For self-similar networks, there exists a fractal dimension of the structure, which should be smaller than the observed geometric dimensionality. The shape of the structure is subsequently scale-invariant. Therefore, there is no characteristic wavelength that represents the overall length scale of the inner microstructures. In contrast, the observed 3-D Ge microsphere has an inner structure of networks, and the connectivity of the network does not exhibit scale-invariance. Rather, the network appears to be composed of self-replicated tetra-

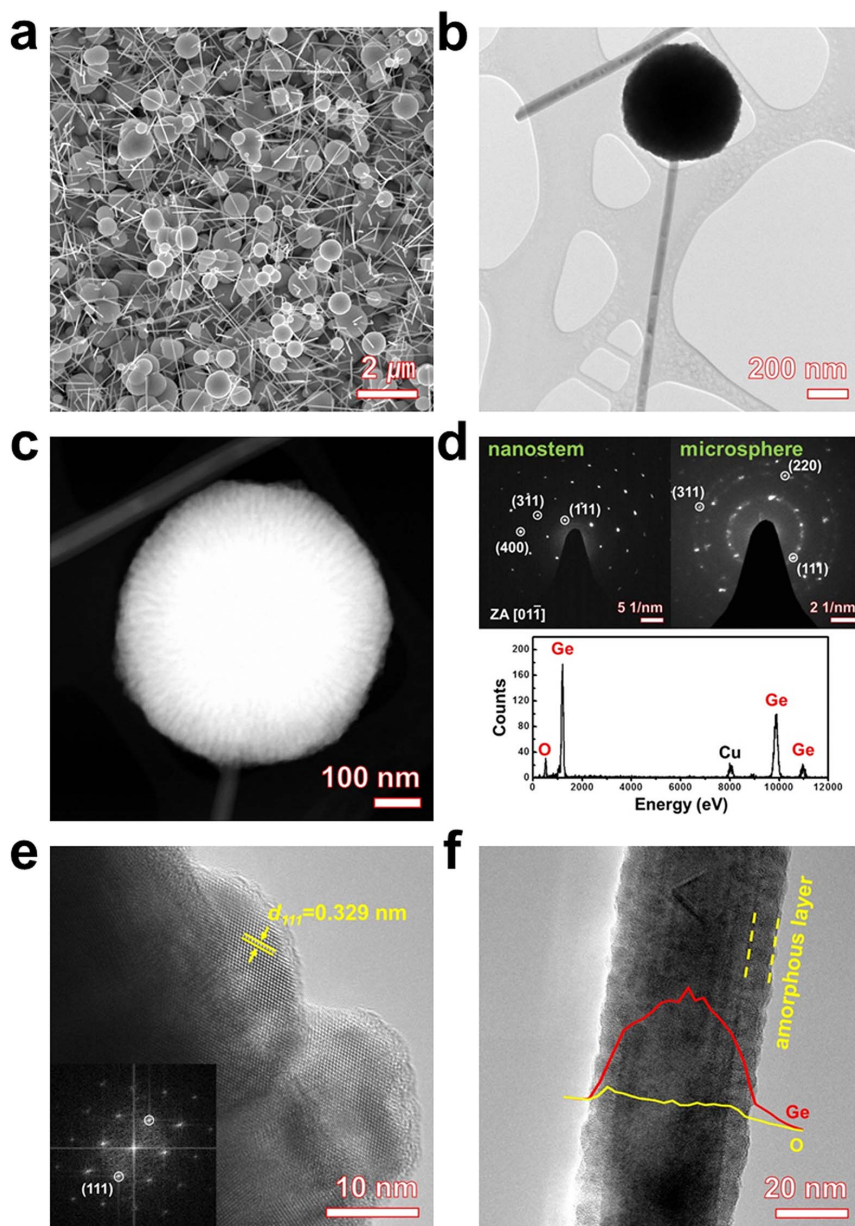


Figure 2 | Morphology of Ge SP-on-NS hybrids. (a) FESEM image of a forest of Ge SP-on-NS hybrids. (b) Low-magnification TEM image and (c) HAADF STEM image of an individual Ge SP-on-NS hybrid. (d) SAED patterns of the Ge nanostem (upper-left part) and Ge microsphere (upper-right part) and representative EDS spectra of the Ge microsphere (bottom part). (e) HRTEM image of the Ge microsphere and its corresponding FFT (inset). (f) TEM image of an individual nanostem and EDS line-scan profile of Ge and O along the cross-sectional line.

hedrons in which polygonal shape joints and pillar shape stems are periodically connected to each other (Supplementary Fig. S6). In this manner, the observed structure is clearly different from a self-similar network (i.e., 3-D Bethe lattice-like structure) both geometrically and topologically.

Some supporting evidence of the self-replicated network structure is found in the FIB cross-sectional images in Figs. 3d,e. In particular, fast Fourier transform (FFT) of the 2-D image of the inner structure indicates the existence of the characteristic wavelength apparent in Fig. 3f. For image analysis, we processed the raw image data obtained from the FIB analysis (Fig. 3d) into the gray-scale image (Fig. 3e) in which the connected parts (i.e., stems and joints) are clearly depicted by using a certain cut-off value of pixels (i.e., 127/255 for the conventional cut-off value). The 2-D FFT image was then calculated from the processed image. As shown in Fig. 3f, the existence of a circular distribution of transformed signals in the reciprocal space is

responsible for the existence of the characteristic wavelength in real space, which corresponds to the regular pore size in the network structure observed in Figs. 3d,e.

To describe how the cross-sectional image of the network structure of the 3-D Ge microspheres is reflected in FIB analysis, we numerically reconstructed the self-replicated 3-D network of the Ge microsphere. An example of the reconstructed 3-D Ge network structure (composed of 4373 joints and 4372 stems) and cross-sectional images viewed from two different directions are shown in Supplementary Fig. S7. Because the tetrahedron is in a cubic diamond lattice (i.e., staggered), we assumed for numerical reconstruction that the self-replication of the tetrahedrons is guided by periodic structure formation. Although not shown in the present study, we found that there are other ways to construct the self-replicated tetrahedrons, such as an eclipsed process, which is not able to account for both the periodic network structures and cross-sectional images.

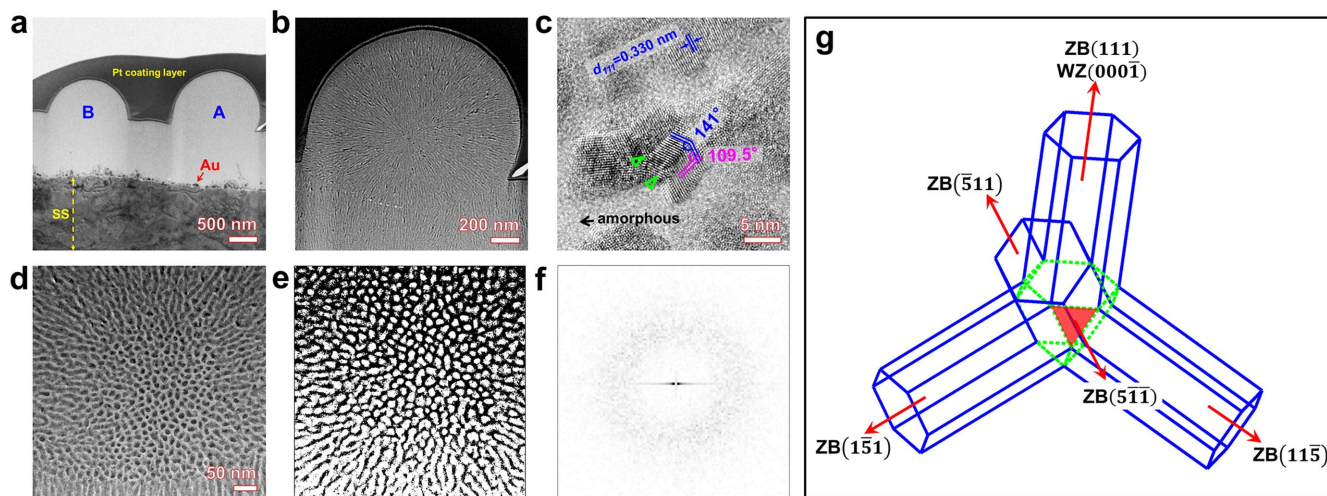


Figure 3 | Cross-sectional morphology of Ge microspheres. (a–d) TEM images of cross-sectional Ge microspheres by FIB to obtain an ultrathin section. The position of (b) is marked by letter “A,” and the position of (d) is marked by letter “B.” (c) HRTEM image of the cross-sectional Ge microsphere (indicated by the letter “B”). (e) A processed image of the cross-sectional area of the Ge microsphere showing the network structure inside the sphere. (f) A 2-D FFT image of the network structure shown in the cross-sectional area of the Ge microsphere in (d). (g) A schematic illustration of the Ge nanostructure composed of four hexagonal stems (outlined with blue solid lines) with a joint which is in a truncated tetrahedron shape (outlined with green dot lines). One of the four triangular planes is depicted with face color red in order to denote different crystalline plane from the four hexagonal planes.

Notably, the reconstructed cross-sectional image viewed from the $\langle 110 \rangle$ direction (Supplementary Fig. S7c) appears to match the observed cross-sectional image in Fig. 3e in that the pore size is regular and the network structure is self-replicated in shape and isotropic in manner, albeit the observed image is in a less regular form than in the periodic manner. The difference between the observation and numerical reconstruction comes from the oxidation of the Ge nanostructures followed by etching. However, we can consider that a cubic diamond structure-like self-replication of tetrahedrons captures the essential characteristics of the 3-D network of the Ge microspheres.

To determine the crystalline structure of the tetrahedral unit for the network structure, we constructed a virtual tetrahedral unit composed of one truncated tetrahedron and four hexagonal prisms (Fig. 3g). It is well known that the $(000\bar{1})$ face of nanocrystalline wurtzite (WZ) is structurally equivalent to the (111) face of the nanocrystalline zinc blend (ZB); therefore, four Ge crystalline hexagonal prisms grown along the ZB (111) , $(11\bar{5})$, $(1\bar{5}1)$, and $(\bar{5}11)$ directions (Fig. 3g) share, without lattice mismatch or structural defects, a joint in the truncated tetrahedron shape that has four hexagonal faces (Fig. 3g). This can be observed in the TEM images in Fig. 3c.

Etching process of GeO_x sheath for Ge MF-on-NS hybrids. Our simple method for fabricating 3-D microscale/1-D nanoscale hybrid structures involves the selective chemical etching of the self-patterned Ge. Etching of the Ge SP-on-NS hybrids in aqueous solution at 50°C results in the selective removal of the amorphous GeO_x sheath and the formation of complex structures consisting of Ge microflowers and Ge nanostems (Figs. 4a,b). EDS analysis shows that Ge is the dominant element, while O is detected in small amounts, further confirming the removal of the encompassing GeO_x sheath (Supplementary Fig. S8f).

The tetrahedral network structure of the Ge microflower was also examined using FESEM and TEM, as shown in Supplementary Fig. S9. We observed the inner structure of the Ge microflowers showing self-replication of tetrahedral-type Ge nanorods (Fig. S9a and b). Furthermore, the hexagonal prism stems were clearly confirmed in TEM images of immature Ge microflowers (Fig. S9c and d). Each of the hexagonal prism stems works as the initial point for the growth of

the next three stems with the formation of another truncated tetrahedron. This repetitive formation of a combination of joints and four stems leads to the repetitive growth of the tetrahedral network structure. By assuming that the growth rates of the stems are equivalent, the Ge network structure gives rise to an isotropic structure, i.e., the spherical shape shown in Figs. 2, 3 and 4.

The FESEM images of the Ge MF-on-NS hybrids are presented in Fig. 4 and Supplementary Fig. S8 and clearly show 3-D spherical microflowers on well-branched, sturdy 1-D nanostems. Compared with the Ge microspheres (Figs. 2a,b), the Ge microflowers are highly porous and fractured, and there are exposed cross sections resulting from the GeO_x etching process. As mentioned above, we can expect that the self-replicated structure formation mechanism for the 3-D Ge network structures would result in a highly porous inner structure of the Ge microsphere after the etching of GeO_x . The geometry of the Ge spherical structure is represented by the radius and porosity (or packing density). To measure these properties, we introduce the generation number of the replication, N , whereby $N = 1$ indicates a simple tetrahedron (the upper left inset of Fig. 4c) and $N = 2$ is for the isotropically replicated tetrahedral structures (the lower right inset of Fig. 4c), and so on. If we can define the origin (center of mass) of the sphere, the radius of the sphere, R_N , which is equal to the maximum distance from the origin to the outmost joints, can be calculated as follows:

$$R_N = \left| \frac{N(\mathbf{c} - \mathbf{a})}{2} \right|, \text{ for } N = 2m, m = 1, 2, 3, \dots \quad (1)$$

$$= \left| \frac{(N+1)\mathbf{c} - (N-1)\mathbf{a}}{2} \right|, \text{ for } N = 2m - 1, m = 1, 2, 3, \dots$$

where \mathbf{c} and \mathbf{a} are the unit vectors for the tetrahedral stems from the origin (Fig. 4c). For large values of N , R_N can be effectively approximated with a linear function of N as follows:

$$\frac{R_N}{L_S} \simeq N \left(\frac{1 - \cos \theta}{2} \right)^{1/2}, \quad (2)$$

where $\theta = 109.47^\circ$, and L_S denotes the center-to-center distance between two neighboring joints in the network. In Fig. 4c, the relationship between R_N and N is clearly linear, as shown in Eq. (2).

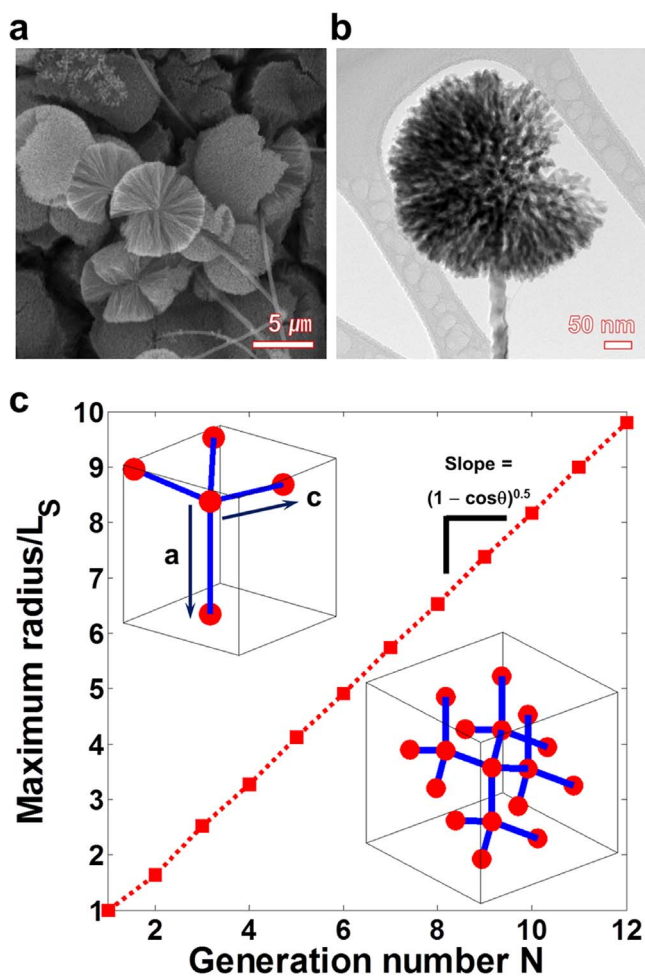


Figure 4 | Morphology of Ge MF-on-NS hybrids. (a) FESEM image of a forest of Ge MF-on-NS hybrids. (b) TEM image of an individual Ge MF-on-NS hybrid. (c) Behavior of the maximum radius of the spherical structure composed of self-replicated tetrahedra, R_N , and the generation number N . The upper-left inset represents the tetrahedral unit with four stems (blue lines) and five joints (red spheres). In the inset, two unit vectors, c and a , are shown. The lower-right inset represents the cubic diamond-like self-replicated tetrahedral structure up to $N = 2$.

Secondly, the porosity or packing density of the spherical structure, ρ , can be easily calculated by considering that the self-replicated tetrahedral structure is mathematically similar to the structure of diamond. For the ideal diamond structure, the maximum ρ is equal to $\rho_M = \pi\sqrt{3}/16$. For the self-replicated tetrahedral structure, however, we can expect that ρ is much smaller than ρ_M , because the four stems originating from each of the joints would occupy most of the space. For convenience, let us define an aspect ratio of the stem, $q \equiv L_S/\sigma$, where σ denotes the unit length of the hexagonal face of the joint. From a simple geometric calculation, we can define the relationship between ρ and q as follows:

$$\rho = \frac{3}{8q^3} \left(\frac{23\sqrt{6}}{12} + 18 \left(q - \frac{\sqrt{6}}{3} \right) \right), \quad (3)$$

and this relationship can be approximated to a simple inversely quadratic relationship such that $\rho \approx 27/4q^2$ for sufficiently large values of q .

Carbon filling of Ge MF-on-NS hybrids. The general morphologies of the carbon-filled Ge MF-on-NS hybrids were investigated by FESEM and HAADF STEM (Figs. 5a–c). The FESEM image shows

that the carbon-filled Ge MF-on-NS hybrids are wrapped in membrane-like carbon, but the Ge MF-on-NS hybrids preserve their morphology (Fig. 5a). Figures 5b–f show the HAADF STEM images and the corresponding EDS analysis of the carbon-filled Ge MF-on-NS hybrids. The HAADF STEM images of the carbon-filled Ge MF-on-NS hybrids are shown in Figs. 5b,c. It is clearly seen that the carbon-filled Ge MF-on-NS hybrids are closely packed with a carbon sheath well into the interior.

To confirm the composition of the formed core/sheath nanostructures, EDS point analyses were performed and are shown in Figs. 5d–f. Besides Ge and C, some other elements are also present in the spectrum. The Cu peaks originate from the grid used for TEM analysis (point #1 of Figs. 5c,d). Figure 5f shows the spectrum of the core of the Ge MF-on-NS hybrids, and Fig. 5e shows the composition of the sheath. Ge and C are observed in both of them; however, the concentration of Ge is found to be quite different. As expected, point #2 in the grayish sheath region showed the presence of mostly C (point #2 of Figs. 5c,e), whereas the Ge and C atoms are mainly grouped in the core of the carbon-filled Ge MF-on-NS hybrids (point #3 of Figs. 5c,f). However, it is difficult to observe the complete structure of the carbon-filled Ge MF-on-NS hybrids because they have a thick carbon sheath and are easily broken off from the Ge nanostems during transfer to the TEM grid. Therefore, we imaged the carbon-filled Ge MF-on-NS hybrids with a thin carbon sheath, which are unbroken after carbon filling (Supplementary Fig. S10).

Supplementary Figure S10b shows the HRTEM image of the dendritic Ge microflower with a thin carbon sheath, which has uniform carbon layers. Points #1–3 are the analysis points of the electron energy-loss spectroscopy (EELS) analysis, which confirms the presence of the carbon sheath (Supplementary Fig. S10c). The EELS spectra near the C-K edge indicate that the Ge nanostem is sheathed by a carbon layer (Supplementary Figs. S10d–f).

Electrochemical performance of Ge MF-on-NS hybrids. To evaluate the electrochemical performance of the Ge SP-on-NS hybrid electrode, typical charge-discharge curves were recorded over 100 cycles at the current rate of 1 C (maximum theoretical capacity of 1623 mA g^{-1} based on 4.4 lithium ions per formula unit of Ge) between 0.01 and 1.2 V (Fig. 6a). The first discharge profile was different from the following reversible cycles, indicating a structural rearrangement in the first discharge process. The first charge curve delivered a capacity of 761 mA h g^{-1} , while the capacity gradually increased over the initial 20 cycles because of the electrochemical activation process. However, the reversible capacities decreased after subsequent cycles (Fig. 6a).

Figure 6b shows that the carbon-filled Ge MF-on-NS hybrid electrodes have a high capacity as well as good capacity retention (96% after 100 cycles). In addition, after 100 cycles, the discharge capacity of this electrode was stable at approximately 1360 mA h g^{-1} at 1 C. On the other hand, the Ge MF-on-NS hybrid electrode fades very rapidly after the initial 10 cycles, and the Ge SP-on-NS hybrid electrode exhibits lower capacities. It is clear that the carbon-filled Ge MF-on-NS hybrids are distinctly superior to the corresponding Ge SP-on-NS and Ge MF-on-NS hybrids.

The charge-discharge curves at the 100th cycle for the three electrodes are shown in Fig. 6c. From the plateau region in each curve, it is determined that a similar reaction occurred in all the electrodes. The Ge SP-on-NS hybrid electrode shows a rapid voltage fading, while the carbon-filled Ge MF-on-NS hybrid electrode exhibits a large voltage plateau with cycling.

Supplementary Figures S11a,b show the FESEM images of the etched and carbon-filled Ge MF-on-NS hybrids after the 100th charge. While severe volume expansion was observed in the Ge MF-on-NS hybrids, little volume change was observed in the carbon-filled Ge MF-on-NS hybrids. As expected, the HAADF STEM images to visualize the material contrast (Supplementary Figs.

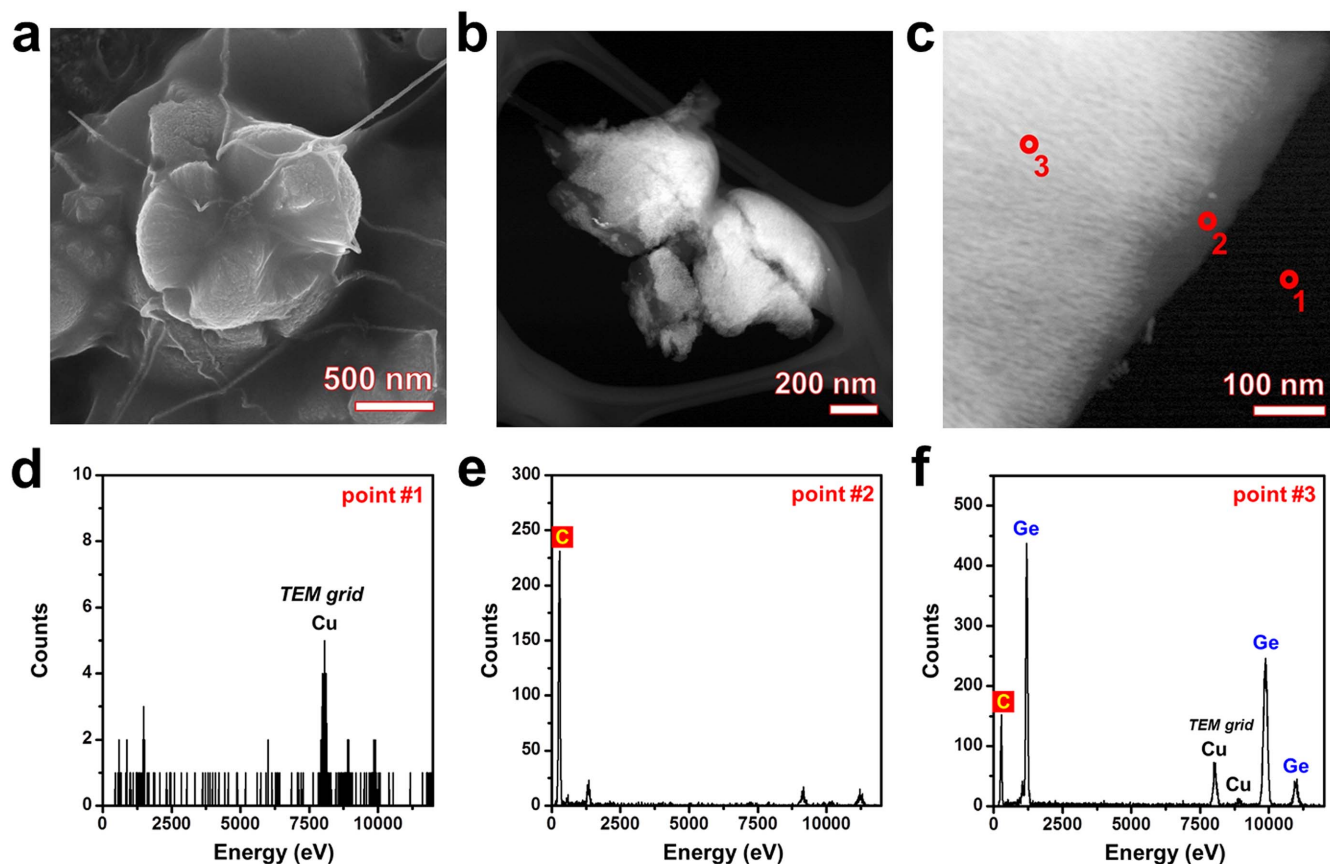


Figure 5 | Morphology of carbon-filled Ge MF-on-NS hybrids. (a) FESEM image of carbon-filled Ge MF-on-NS hybrids. HAADF STEM images at (b) low magnification and (c) high magnification. The empty space in the Ge MF-on-NS hybrids is completely filled with carbon. Representative EDS spectra with HAADF STEM images obtained from points (d) #1, (e) #2, and (f) #3. The EDS spectra corresponding to point #3 indicate the presence of carbon. It is clear that the amorphous sheath consisted mainly of carbon.

S11c,d) reveal that the carbon-filled Ge MF-on-NS hybrids retained the morphology of the dendritic Ge nanorods. The corresponding SAED pattern of the carbon-filled Ge MF-on-NS hybrids (inset of Supplementary Fig. S11d) exhibits some clear concentric rings and some bright spots, indicating the polycrystalline nature after the charging cycle compared to the etched Ge MF-on-NS hybrids (inset of Supplementary Fig. S11c). The HRTEM image of the bare and carbon-filled Ge MF-on-NS hybrids in the fully delithiated state further confirms that the Ge MF-on-NS hybrids are Ge nanocrystals with a diameter of *ca.* 5 nm (red square) embedded in an amorphous matrix, which is clearly distinguished from the particles by FFT (Supplementary Fig. S12a). However, the carbon-filled Ge MF-on-NS hybrids retain much of their crystallinity (Supplementary Fig. S12b).

Furthermore, the content of carbon was estimated to be $\sim 22\%$ by measuring precise masses before and after carbon filling using a microbalance. Based on the content of carbon, the theoretical capacity of carbon-filled Ge MF-on-NS hybrids can be calculated to be 1348 mA h g^{-1} (theoretical capacity = $1623 \text{ mA h g}^{-1} \times 0.78 + 372 \text{ mA h g}^{-1} \times 0.22$). The reversible capacity of carbon-filled Ge MF-on-NS hybrids was still large value, $\sim 1114 \text{ mA h g}^{-1}$ ($\sim 83\%$ of the calculated theoretical capacity) after 100 cycles, as shown in Fig. R1–4.

Further electrochemical information is provided by the cyclic voltammetry (CV) measurements of the bare and carbon-filled Ge MF-on-NS hybrid electrodes (Supplementary Fig. S14). The lithiation and delithiation peaks appeared for the lithium alloying and dealloying processes along with the peaks reported for $\text{Ge}^{34,35}$. The Ge MF-on-NS hybrid electrode shows a reaction region with lithiation

peaks at *ca.* 0.12 and *ca.* 0.32 V during the 10th and the 50th discharge; a single distinct delithiation peak is evident at *ca.* 0.54 V during the first charge, while two broad delithiation peaks are observed at *ca.* 0.41 and *ca.* 0.52 V during the 50th charge (Supplementary Fig. S14a), which is consistent with the result of the charge-discharge curves (Fig. 6a). For the carbon-filled Ge MF-on-NS hybrid electrode, a very large and sharp peak at *ca.* 0.51 V is observed during the 50th charge, which is shifted to a lower voltage ($0.53 \text{ V} \rightarrow 0.51 \text{ V}$) during from 10th cycle to 50th cycle, and the lithiation peak at *ca.* 0.12 V at the 10th discharge is observed to shift to 0.14 V during the 50th discharge (Supplementary Fig. S14b).

The rate capability performance is shown in Fig. 6d. After the carbon-filled Ge MF-on-NS hybrid electrode had been cycled for 10 cycles at a rate of 0.2 C, the current densities were increased stepwise to 10 C. A highly stable reversible capacity of 850 mA h g^{-1} was obtained at the highest current density of 10 C. After 40 cycles under various conditions, the carbon-filled Ge MF-on-NS hybrid electrode recovers approximately 97% of the initial capacity at 1 C.

Discussion

Growth mechanism of dendritic Ge microflower-on-nanostem hybrids. Based on the morphology characteristics and growth conditions of the Ge MF-on-NS hybrids, we propose the following growth process.

To determine how the straight Ge nanowire undergoes the structural transformation (or spontaneous polytypism) to the self-replicating tetrahedral form, we compared the free energy of the two structures based on the surface energy of the crystalline face of the

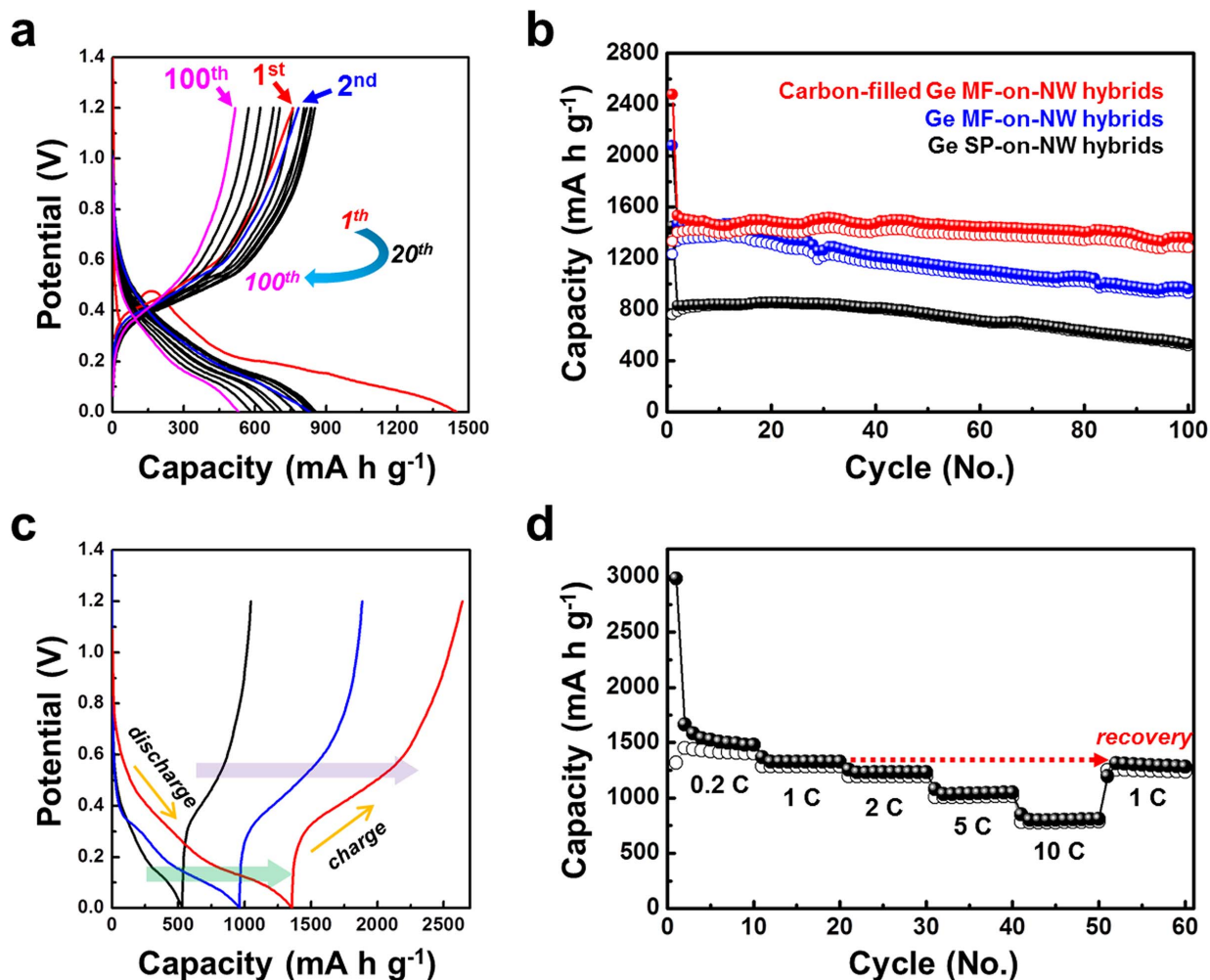


Figure 6 | Electrochemical performance of Ge hybrid series electrodes. (a) Typical discharge-charge curves of Ge SP-on-NS hybrid electrode at a current rate of 1 C. (b) Variation of the discharge-charge specific capacity versus the cycle number for the Ge SP-on-NS (black), Ge MF-on-NS (blue), and carbon-filled Ge MF-on-NS hybrid electrodes at 1 C. (c) The 100th discharge-charge curves of the Ge SP-on-NS (black), Ge MF-on-NS (blue), and carbon-filled Ge MF-on-NS hybrid electrodes at 1 C. (d) Cycling performance at various C rates of the carbon-filled Ge MF-on-NS hybrid electrode.

structure, F_1/F_2 , where F_1 is for the straight wire, and F_2 is for the tetrahedral with the truncated tetrahedron joint. With a simple geometrical calculation, F_1/F_2 can be written as follows:

$$\frac{F_1}{F_2} = 1 + \frac{\sqrt{3}\bar{\gamma} - 6C}{6L}, \quad (4)$$

where $\bar{\gamma}$ denotes the ratio of the surface free energies of the ZB (111) plane (i.e., the triangular face of the truncated tetrahedron, Fig. 3g) and the ZB (511) plane faces (i.e., the hexagonal plane for the interface between the stem and the joint), C is a constant ($C = 23\sqrt{6}/54$) calculated from the volume conservation, and L is the ratio between the length of the wire before the structural transformation and the lattice constant, respectively. It should be noted that $\bar{\gamma}$ does not necessarily equal unity, because the two planes of the truncated tetrahedrons have different crystalline periodicities and subsequently different number densities of atoms on the surface of the plane. From Eq. (4), we find that the tetrahedral form is energetically preferred to the wire form when $\bar{\gamma} \leq 23\sqrt{2}/9 \sim 3.61$, although the surface free energy difference would be relatively negligible as the initial length of the wire is too long. In other words, for a sufficiently short initial wire, it is highly probable for the wire to undergo the structural transformation without any change in the crystalline structure from the wire to the tetrahedrons.

Improving the electrochemical performance of Ge microflower-on-nanostem hybrids. Ge is considered an ideal candidate for anode materials of lithium ion batteries (LIBs) with a high theoretical specific capacity of 1623 mA h g^{-1} . Despite the high theoretical capacity of Ge anodes, capacity fading during cycling performance in a lithium-alloying reaction system still occurs, chiefly because of the mechanical deterioration of the active materials, e.g., cracking and pulverization, caused by large volume changes (370%) when the lithium ions are inserted and extracted in the active matrix^{36,37}. This phenomenon brings about an electrical contact loss between the active materials and the electronic paths, resulting in capacity loss during reversible cycling.

We believe that highly ordered and aligned 3-D fractal nanorod network structures have significant advantages in their kinetics and electronic conduction during the lithium-alloying process compared to their more bulky counterparts^{21,27}. Our thermal evaporation process was found to assist the adhesion between the Ge MF-on-NS hybrids and the SS substrate because of the interfacial Fe-Ge alloy formation, as determined from the XRD pattern of the Ge SP-on-NS hybrids (Supplementary Fig. S2).

Moreover, we suppose that the improvement in the cycling performance of the carbon-filled Ge MF-on-NS hybrids is related to the increased mechanical stability by carbon filling, compared to the unfilled materials, as evidenced by the results of the electrodes after the 100th charge (Supplementary Fig. S11 and S12). The peak at



0.51 V in CV measurement is attributed to Li-dealloying reaction in Ge. The carbon filled sample showed enhanced reaction currents, which is consistent with the Li-storage capacity data by galvanostatic cycling³⁸. Consequently, the carbon-filled Ge MF-on-NS hybrid electrode exhibits excellent electrochemical performance in terms of cycle stability and rate capability.

Methods

Preparation of Ge SP-on-NS hybrids. The Ge SP-on-NS hybrids were synthesized by the thermal evaporation of Ge powders (99.99%) placed at the center of a quartz tube in a horizontal furnace. Under a constant flow of nitrogen at 150 sccm in vacuum, the furnace was heated to 650 °C for 15 min and then cooled to room temperature. We placed a coated stainless steel substrate with an Au catalyst layer (10 nm) downstream of the tube furnace.

Preparation of Ge MF-on-NS hybrids. For etching the GeO₂ sheath, an aqueous solution of 100 mL distilled water and acetone (2.5/7.5, v/v, acetone/H₂O) was mixed with 0.2 mL of sulfuric acid. The as-prepared Ge SP-on-NS hybrids were soaked in 50 mL of the aqueous solution for 150 min at 40 °C. The sample was then washed several times with ethyl alcohol and isopropyl alcohol. Finally, the washed sample was dried under vacuum at 60 °C for 30 min.

Preparation of carbon-filled Ge MF-on-NS hybrids. Citric acid (C₆H₈O₇) was dissolved in 200 mL of absolute ethyl alcohol. The solution was poured on the Ge MF-on-NS hybrids and then baked on a hot plate at 90 °C. Finally, the carbon-filled Ge MF-on-NS hybrids were obtained via heat treatment from the decomposition of the citric acid. Citric acid was chosen as the carbon source because of its low decomposition temperature (175 °C) and low oxygen content.

Material characterization. The morphology, composition, and crystalline phase of all the samples synthesized in this work were characterized by field emission scanning electron microscopy (FESEM; Nova 600 NanoLab, FEI), high-resolution transmission electron microscopy (HRTEM; Tecnai G2, FEI), and X-ray diffraction analysis (XRD; D8, Bruker AXS).

Electrochemical characterization. The electrochemical performance was evaluated by assembling Swagelok-type half-cells using lithium metal foil as the counter electrode. A separator film (Celgard 2400) and liquid electrolyte composed of ethylene carbonate and dimethyl carbonate (1/1, v/v) with 1-M LiPF₆ (Techno Semichem Co., Ltd.) were also used. The assembled cells were galvanostatically cycled between 0.01 and 1.2 V using an automatic battery cyclers (WBCS 3000, WonATech, Korea).

- Tiwari, J. N., Tiwari, R. N. & Kim, K. S. Zero-dimensional, one-dimensional, two-dimensional and tree-dimensional nanostructured materials for advanced electrochemical energy devices. *Prog. Mater. Sci.* **57**, 724–803 (2012).
- Milliron, D. J. *et al.* Colloidal nanocrystal heterostructures with linear and branched topology. *Nature* **430**, 190–195 (2004).
- Rathmell, A. R., Bergin, S. M., Hua, Y.-L., Li, Z.-Y. & Wiley, B. J. The growth mechanism of copper nanowires and their properties in flexible, transparent conducting films. *Adv. Mater.* **22**, 3558–3563 (2010).
- Chan, C. K. *et al.* High-performance lithium battery anodes using silicon nanowires. *Nature nanotech.* **3**, 31–35 (2008).
- Ko, Y.-D. *et al.* Sn-induced low-temperature growth of Ge nanowire electrodes with a large lithium storage capacity. *Nanoscale* **3**, 3371–3375 (2011).
- Ko, Y.-D., Kang, J.-G., Park, J.-G., Lee, S. & Kim, D.-W. Self-supported SnO₂ nanowire electrodes for high-power lithium-ion batteries. *Nanotechnology* **20**, 455701 (2009).
- Park, W. I., Jun, Y. H., Jung, S. W. & Yi, G.-C. Excitonic emissions observed in ZnO single crystal nanorods. *Appl. Phys. Lett.* **82**, 964–966 (2003).
- Kim, F., Kwan, S., Akana, J. & Yang, P. Langmuir-Blodgett nanorod assembly. *J. Am. Chem. Soc.* **123**, 4360–4361 (2001).
- Vigderman, L., Khanal, B. P. & Zubarev, E. R. Functional gold nanorods: synthesis, self-assembly, and sensing applications. *Adv. Mater.* **24**, 4811–4841 (2012).
- Cao, Q. & Rogers, J. A. Ultrathin films of single-walled carbon nanotubes for electronics and sensors: a review of fundamental and applied aspects. *Adv. Mater.* **21**, 29–53 (2009).
- Guo, J., Xu, Y. & Wang, C. Sulfur-impregnated disordered carbon nanotubes cathode for lithium-sulfur batteries. *Nano Lett.* **11**, 4288–4294 (2011).
- Sherry, L. J., Chang, S.-H., Schatz, G. C. & Van Duyne, R. P. Localized surface plasmon resonance spectroscopy of single silver nanocubes. *Nano Lett.* **5**, 2034–2038 (2005).
- Chen, M., Kim, J., Liu, J. P., Fan, H. & Sun, S. Synthesis of FePt nanocubes and their oriented self-assembly. *J. Am. Chem. Soc.* **128**, 7132–7133 (2006).
- Léonard, F. & Talin, A. A. Electrical contacts to one- and two-dimensional nanomaterials. *Nature nanotech.* **6**, 783–783 (2011).
- Okamoto, H., Sugiyama, Y. & Nakano, H. Synthesis and modification of silicon nanosheets and other silicon nanomaterials. *Chem. Eur. J.* **17**, 9867–9887 (2011).

- Yao, Y. *et al.* interconnected Silicon hollow nanospheres for lithium-ion battery anodes with long cycle life. *Nano Lett.* **11**, 2949–2954 (2011).
- Cao, X., Xie, Y. & Li, L. Crystallization of amorphous colloids: an effective approach for the rapid and large-scale preparation of antimony sulfide dendrites. *J. Solid State Chem.* **177**, 202–206 (2004).
- Cao, G. *et al.* Microscopy investigation of Ag-TCNQ micro/nanostructures synthesized via two solution routes. *Micron* **36**, 285–290 (2005).
- Gu, X. *et al.* Controlled growth of porous α -Fe₂O₃ branches on β -MnO₂ nanorods for excellent performance in lithium-ion batteries. *Adv. Funct. Mater.* **23**, 4049–4056 (2013).
- Elias, J. *et al.* Hollow urchin-like ZnO thin Films by electrochemical deposition. *Adv. Mater.* **22**, 1607–1612 (2010).
- Xiao, Y. *et al.* 3D hierarchical Co₃O₄ twin-spheres with an urchin-like structure: large-scale synthesis, multistep-splitting growth, and electrochemical pseudocapacitors. *Adv. Funct. Mater.* **22**, 4052–4059 (2012).
- Jeon, S. & Yong, K. A novel composite hierarchical hollow structure: one-pot synthesis and magnetic properties of W₁₈O₄₉-WO₂ hollow nanourchins. *Chem. Commun.* 7042–7044 (2009).
- Lee, C. W. *et al.* Heteroepitaxial growth of ZnO nanosheet bands on ZnCo₂O₄ submicron rods toward high-performance Li ion battery electrodes. *Nano Res.* **6**, 348–355 (2013).
- Wang, C. *et al.* Large scale synthesis and gas-sensing properties of anatase TiO₂ three-dimensional hierarchical nanostructures. *Langmuir* **26**, 12841–12848 (2010).
- Cheng, C., Tay, Y. Y., Hng, H. H. & Fan, H. J. Solution heteroepitaxial growth of dendritic SnO₂/TiO₂ hybrid nanowires. *J. Mater. Res.* **26**, 2254–2260 (2011).
- Park, S. *et al.* Tailoring nanobranches in three-dimensional hierarchical rutile heterostructures: a case study of TiO₂-SnO₂. *CrystEngComm* **15**, 2939–2948 (2013).
- Xu, P. & Yu, B. The scaling laws of transport properties for fractal-like tree networks. *J. Appl. Phys.* **100**, 104906 (2006).
- Jeon, N., Dayeh, S. A. & Lauhon, L. J. Origin of poly type formation in VLS-grown Ge nanowires through defect generation and nanowire kinking. *Nano Lett.* **13**, 3947–3952 (2013).
- Yeh, C.-Y., Lu, Z. W., Froyen, S. & Zunger, A. Zinc-blende-wurtzite polytypism in semiconductors. *Phys. Rev. B* **46**, 10086–10097 (1992).
- Manna, L., Milliron, D. J., Meisel, A., Scher, E. C. & Alivisatos, A. P. Controlled growth of tetrapod-branched inorganic nanocrystals. *Nature Mater.* **2**, 382–385 (2003).
- Ehman, M. F., Vedam, K., White, W. B. & Faust, J. W. JR. Characterization of thin surface films on germanium in various solvents by ellipsometry. *J. Mater. Sci.* **6**, 969–973 (1971).
- Pei, L. Z. *et al.* Large-scale synthesis and growth conditions dependence on the formation of CuGeO₃ nanowires. *Mate. Chem. Phys.* **130**, 104–122 (2011).
- Rosales, I. *et al.* Raman analysis of an impacted α -GeO₂-H₂O mixture. *High Pre. Res.* **32**, 396–404 (2012).
- Yan, C., Xi, W., Si, W., Deng, J. & Schmidt, G. S. High conductive and strain-released hybrid multilayer Ge/Ti nanomembranes with enhanced lithium-ion-storage capability. *Adv. Mater.* **25**, 539–544 (2013).
- Rudawski, N. G. *et al.* Ion beam-mixed Ge electrodes for high capacity Li rechargeable batteries. *J. Power Sources* **223**, 336–340 (2013).
- Chan, C. K., Zhang, X. F. & Cui, Y. High capacity li ion battery anodes using Ge nanowires. *Nano Lett.* **8**, 307–309 (2008).
- Hwang, I.-S. *et al.* A binder-free Ge-nanoparticle anode assembled on multiwalled carbon nanotube networks for Li-ion batteries. *Chem. Commun.* **48**, 7061–7063 (2012).
- Wang, H. *et al.* Hydrothermal synthesis and electrochemical properties of tin titanate nanowires coupled with SnO₂ nanoparticles for Li-ion batteries. *CrystEngComm* **16**, 7529–7535 (2014).

Acknowledgments

This research was supported by Basic Science Research Program through the National Research Foundation of Korea(NRF) funded by the Ministry of Science, ICT and future Planning(2012R1A2A2A01045382 and 2010-0029027). This research was also supported by the KIST institutional program (2E24572).

Author contributions

G.-H.L. performed, analyzed the experiments and drafted the manuscript. S.J.K., performed theoretical analysis on the growth mechanism and drafted the manuscript. K.-S.P. and J.-G.K. performed material characterization. S.L. designed the measurement of precise mass using a microbalance. J.-C.K. carried out drawing illustrations for experimental concepts. H.-W.S. participated in electrochemical tests. J.-G.P. and D.-W.K. conceived and designed the study, led the discussion of the results, and performed the final edits of the manuscript. All authors made critical contributions to the work, discussed the results and commented on the manuscript.

Additional information

Supplementary information accompanies this paper at <http://www.nature.com/scientificreports>



Competing financial interests: The authors declare no competing financial interests.

How to cite this article: Lee, G.-H. *et al.* Germanium microflower-on-nanostem as a high-performance lithium ion battery electrode. *Sci. Rep.* **4**, 6883; DOI:10.1038/srep06883 (2014).



This work is licensed under a Creative Commons Attribution-NonCommercial-NoDerivs 4.0 International License. The images or other third party material in this article are included in the article's Creative Commons license, unless indicated otherwise in the credit line; if the material is not included under the Creative Commons license, users will need to obtain permission from the license holder in order to reproduce the material. To view a copy of this license, visit <http://creativecommons.org/licenses/by-nc-nd/4.0/>